ANALYSIS OF SCHOTTKY DIODE FAILURE MECHANISMS DURING EXPOSURE TO AN ELECTRON BEAM PULSE USING TCAD SIMLULATION

By

Jeremy Ralston-Good

Thesis

Submitted to the Faculty of the

Graduate School of Vanderbilt University

in partial fulfillment of the requirements

for the degree of

MASTER OF SCIENCE

in

Electrical Engineering

May, 2003

Nashville, Tennessee

Approved by:

Professor Ronald D. Schrimpf

Professor Greg Walker

AKNOWLEDGEMENTS

I would like to thank my family and friends for their support. Also, I would like to express my sincere gratitude to Dr. Veillette, Dr. Schrimpf and Dr. Walker for their guidance and encouragement.

TABLE OF CONTENTS

Page

ACKNOWLEDGMENTS ii

LIST OF FIGURES v

LIST OF TABLES vi

Chapter

I. INRODUCTION 1

Overview 2
General Description of Power Schottky Diodes 3

II. EXPERIMENT 7

Introduction 7
Dosimetry Description 7
Test Fixture Description 9
Test Procedure 10
Experimental Results of 150-Volt Device 10
Experimental Results of 45-Volt Device 13
Experimental Supplement 13
Conclusions from Experiment 14

III. SIMULATION MODEL 15

Simulation Overview 15
Process Modeling 15
Device Modeling 16
Fundamental Semiconductor Equations 16
The Drift-Diffusion Transport Model 17
Mobility Model 17
Carrier Generation-Recombination Models 18
Auger Recombination Model 20
Impact Ionization Models 20
Transient Modeling of Heat Generation and Conduction 22

Boundary Conditions 23

IV. RESULTS AND DISCUSSION 25

Results and Discussion overview 25
Simulation Structure 25
Simulation Results 26
Breakdown Discussion 30
Device Survivability Discussion 33

V. CONCLUSIONS 37

REFERENCES 39

LIST OF FIGURES

Figure Page

1.1 Illustration of Schottky rectifier Cross-Section 2

1.2 Schottky rectifier structure and its band diagram, from the cutline in Fig 1.1 3

1.3(a) Schottky Rectifier edge terminations: metal field plate structure 5

1.3(b) Schottky Rectifier edge terminations: diffused guard ring structure 5

1.4 Illustration of circuit level model for device under examination 5

2.1 PIN diode circuit. A TLD is placed at the approximate Device Under Test (DUT) location to determine the dose of each pulse to calibrate the PIN diode 8

2.2. Test circuit used to measure photocurrent response 9

2.3 Photocurrent response, I_p, of an IR12CGQ150 when subjected to a 20-ns, $5x10^9$ rd(Si)/s electron pulse and reverse bias of 100 volts 11

2.4 Photocurrent response, I_p, of an IR12CGQ150 when subjected to a 20-ns, $1.3x10^{10}$ rd(Si)/s electron pulse and reverse bias of 100 volts 11

2.5 Peak current response, I_{pp}, measured from an IR12CGQ150 when reverse biased at 60, 100, and 150 Volts over a wide range of dose rates 12

2.6 Die photograph and zoom showing failure at the guard ring as a result of electron pulse at guard ring 12

2.7 Photocurrent response, Ip, of an IR22CGQ045 when subjected to a 20-ns, $1.1x10^{10}$ rd(Si)/s electron pulse and reverse bias of 45 volts 13

2.8(a) SEM Cross-sectional of contact aluminum spike through to the epi layer from a device that failed under test 14

2.8(b) Diagram of relevant features of photograph 2.8(a) 16

4.1 Simulation structure models the guard ring portion of the device 26

4.2 Pre-pulse Potential contours of Schottky diode biased at –150 Volts 27

4.3 Cutline showing potential gradients across guard ring region 27

4.4 Time Sequence showing the formation of the electron bridge, effectively shorting the guard ring to the n^+ substrate (a) t=0, (b) t=0.01 ns, (c) t=0.31ns, (d) t=7.7ns 28

4.5 Depletion region (a) before and (b) 0.31 nanoseconds into the pulse 29

4.6 Local temperatures at t=17ns after pulse begins, zoomed to guard ring 29

4.7 Intrinsic temperature, T_i, versus doping level of n-type substrate. Doping level of n-type substrate of 150-volt device shown by a red line 31

4.8 Cutline through p+n junction showing doping concentrations versus the thermally generated intrinsic carrier concentration, N_i. From this Figure it is evident that N_i is much greater than the n-type epi layer, and is responsible for junction breakdown 32

4.9 Illustration of p+n junction and a plot of its simulated current vs. temperature 33

4.10(a) Current and peak temperatures versus time for the 150-volt device reverse-biased at 150 Volts 34

4.10(b) Current and peak temperatures versus time for the 150-volt device reverse-biased at 75 Volts 34

4.11 Current and peak temperatures versus time (a) for the 150-volt device reverse-biased at 150 Volts and (b) the 150-volt device reverse-biased at 75 Volts 35

4.13 Plot of simulated temperatures generated at the guard-ring pn junction during and shortly after a 20 ns, $5x10^{11}$ rd(Si)/s pulse are shown for the 150-volt and 45-volt rated devices 36

LIST OF TABLES

Table Page

2.1 Characteristics of Power Schottky Diodes Used in Experiment.. 7

2.2 Dosimeter Description 9

3.1 Parameter Values for Equations 3.17 and 3.18 20

3.2 Parameter Values for Equation 3.19.. 20

3.3 Parameters Values for Equations 3.23-3.26.. 21

CHAPTER I

INTRODUCTION

1.1 Motivation

Until recently, power Schottky diodes were thought to be insensitive to ionizing radiation, including total dose and displacement damage effects. Schottky diodes were expected to exhibit relatively small photocurrents because the depletion layer under the anode contact was expected to be narrow, as compared to a conventional pn junction diode.

A recent study by Titus, et al. reported the photocurrents of reverse-biased power Schottky diodes during exposure to 20 ns, 40-MeV pulses[1]. An illustration of the device structure is shown in Figure 1.1. At beam intensities greater than 10^{10} rd(Si)/s, some devices were observed to fail catastrophically during the pulse or shortly thereafter. This work is an extension of the previous study to identify the physical mechanisms responsible for the localized breakdown.

In this work, numerical process and device simulation tools are used to analyze the mechanisms governing the dose rate response of power Schottky diodes. Simulations suggest that the diodes fail at the guard ring edge due to a depletion region collapse that effectively shorts the guard ring to the substrate, leading to high current densities and thermal runaway. Numerical simulations are also used to examine techniques to increase survivability.

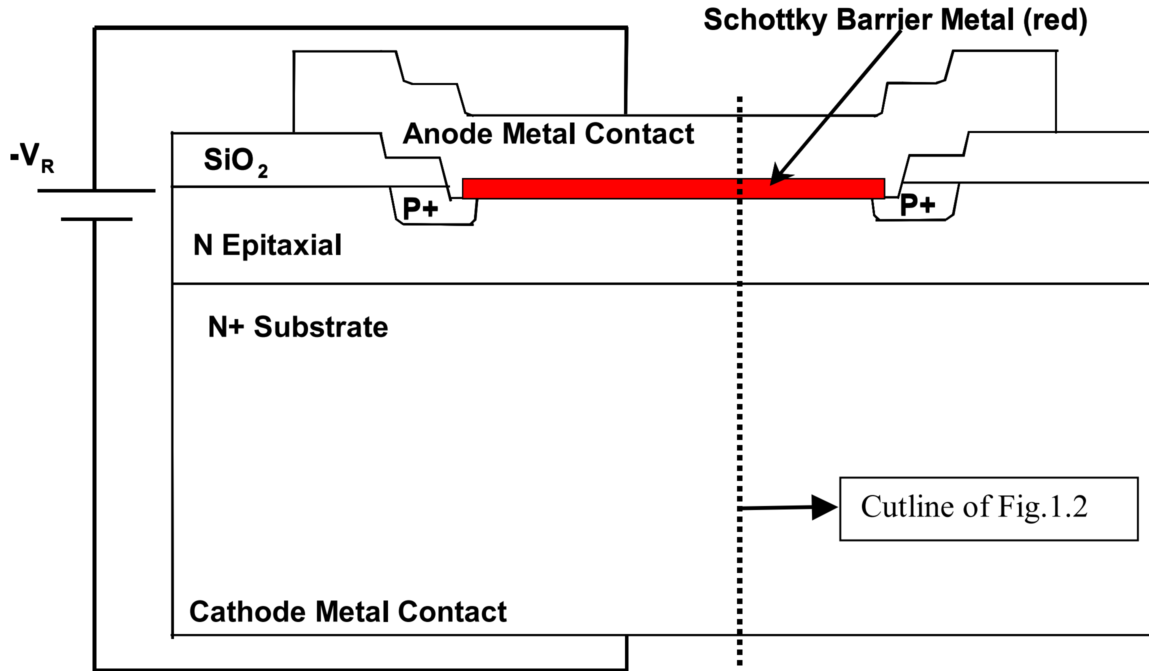

Figure 1.1. Illustration of Schottky rectifier cross-section

1.2 Overview

Semiconductor devices are often required to operate under adverse conditions including both man-made and natural radiation. Three examples of typical radiation environments are:

1. Space environments consisting of galactic and cosmic rays
2. Radiation environments in and around a nuclear reactor system
3. Environments resulting from nuclear weapon detonation

The radiation environments listed above are each characterized by the fluence and energy distribution of particles and photons. The effects on semiconductor devices by each radiation type are well documented[2]. Ionizing radiation effects are generally classified as follows:

1. Bulk displacement damage due to neutrons
2. Total dose effects due to the total radiation dose (energy absorbed by ionization per unit mass of the material) accumulated over time.
3. Single charged particle ionizing effects (SEE)
4. Photocurrent effects due to bulk generation of electron-hole pairs by ionizing radiation dose rate (energy absorbed by ionization per unit mass of the material per unit time).

This work is concerned with photocurrents, specifically the modeling of the dose rate response of reverse-biased power Schottky diodes following the method of experiments performed by Titus, et al.[1].

1.2 General Description of Power Schottky diodes

Schottky diodes are majority carrier devices that exhibit a rectifying characteristic and have a low on-state voltage. The fabrication of Schottky diodes can be accomplished using different metals, such as Molybdenum, Platinum, Palladium, etc. The Schottky barrier is formed on top of an n-type epitaxial layer. The Schottky barrier height ϕ_{Bn} is dependent on the work function of the metal. The reverse blocking characteristics are identical for all metals because the reverse leakage current increases as the magnitude of the reverse bias increases. This soft breakdown characteristic causes excess power dissipation under larger reverse-bias conditions. A Schottky rectifier structure and band diagram are illustrated in Figure 1.2, extracted along the cutline shown in figure 1.1.

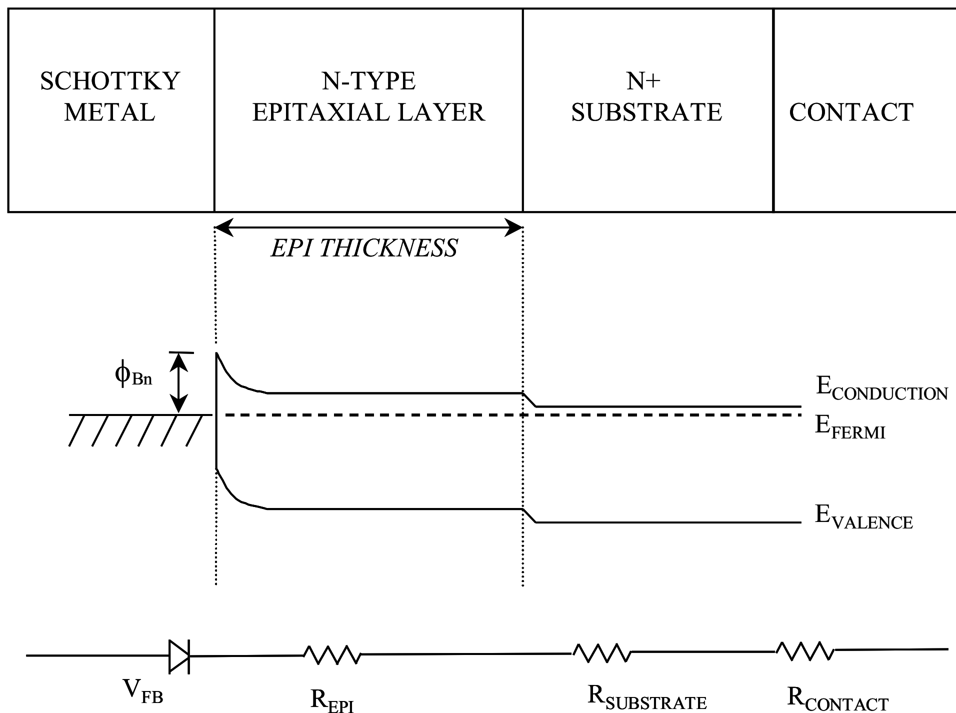

Figure 1.2. Schottky rectifier structure and its band diagram, from the cutline in Fig 1.1.

When a Schottky barrier is reverse biased, a depletion region extends into the epitaxial layer (epi layer) semiconductor region. The reverse blocking voltage characteristic of the Schottky diode is dependent on the epi layer thickness, t_E, and its doping concentration, N_D. The current carrying capability of the device is adjusted by the die area. The epi layer is necessarily scaled with depletion width, W_D, induced by the reverse-bias conditions. The depletion width and the epi layer doping concentration are scaled with the breakdown voltage, given here for an ideal parallel–plane junction[4]

$$W = \left[\frac{2\varepsilon_{SI}\varepsilon_0}{qN_D} (V_B) \right]^{1/2} \tag{0.1}$$

$$N_D = \left[\frac{1.77 \times 10^{18}}{(V_B)^{1.33}} \right]^{1/2} \tag{0.2}$$

where V_B is the breakdown voltage, as set by design requirements, and the junction built-in voltage is negligible compared to the applied voltage.

When a reverse bias is applied across a Schottky barrier, a large leakage current results. This leakage is caused by the large saturation current density, J_S. J_S increases with a reduction in the Schottky barrier height and increases with temperature. When a reverse bias is applied across a Schottky barrier, the reverse current J_R can be written as

$$J_R = AT^2 e^{-(q\phi_{Bn}/kT)} \left[e^{-(qV_R/kT)} - 1 \right] \tag{0.3}$$

where T is the absolute temperature, q is the electronic charge, k is Boltzmann's constant, ϕ_{Bn} is the barrier height between the metal and N-type semiconductor, V_R is the reverse voltage applied, and A is the effective Richardson constant.

In application, the actual breakdown voltage of a Schottky diode is typically about one-third that for the abrupt parallel plane junction because of the limitations inherent to the Schottky barrier termination edge. Electric field crowding occurs at the edge of the Schottky barrier during reverse biasing, leading to high leakage current and breakdown well below the infinite parallel-plane breakdown voltage (soft breakdown). The reverse breakdown voltage can be increased with improved edge termination techniques. Figure 1.3 illustrates two commonly used approaches to edge termination.

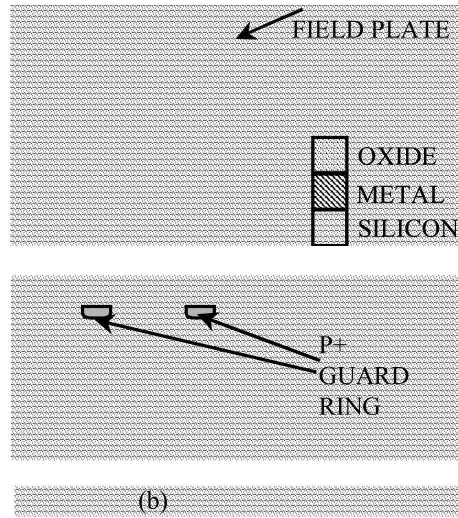

Figure 1.3. Schottky rectifier edge terminations: (a) metal field plate structure; (b)diffused guard ring structure.

For this work, simulated 45-volt and 150-volt rated device structures were derived in cooperation with the device manufacturer, International Rectifier Corporation. The diode studied employs a p+ diffused guard ring, with an overlying field plate as an edge termination to the Schottky barrier metal as shown in Figure 1.1. The field plate is designed to reduce the depletion layer curvature and the electric field magnitude at the termination edge, raising the breakdown voltage closer to that of an ideal planar diode. It is noted that the guard ring structure has a circuit model of two p+n junctions formed in parallel with the Schottky barrier metal as shown in Figure 1.4.

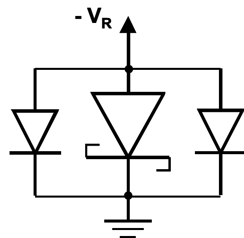

Figure 1.4. Illustration of circuit level model for device under examination.

The experimental study and results for this work, as performed by Titus, et al. is described in Chapter II.

CHAPTER II

EXPERIMENT

2.1 Introduction

For the first time, the dose rate response of power Schottky diodes is reported by Titus, et al[1]. The prompt photocurrent response of commercially available reverse-biased diodes during exposure to 20-ns, 40-MeV electron pulses was recorded over a range of beam intensities from 10^8 to $4x10^{11}$ rd(Si)/s by Titus, et al. At beam intensities greater than 10^{10} rd(Si)/s, some devices were observed to fail catastrophically during the pulse or shortly thereafter.

In this study, International Rectifier power Schottky diodes were examined for dose rate sensitivity. These diodes have the characteristics listed in Table 2.1.

Table 2.1
Characteristics of Power Schottky Diodes Used in Experiment

Part Type	Package Type	V_R (V)	I_F(A)	Die Area (in^2)
12CGQ150	TO-254	150	35	0.0156
22CGQ045	TO-254	45	35	0.0225
5EQ100	LCC	100	8	0.0156
22GQ100	TO-254	100	30	0.0400
15CGQ100	TO-254	100	35	0.0156

2.2 Dosimetry Description

PIN diodes are used as radiation detectors. PIN diodes use heavily doped p-type and n-type regions separated by an intrinsic region. Dosimetry is calibrated to a cobalt-60 source, traceable to National Institute of Standards and Technology and standard dosimetry practices as described by[5]. In this experiment, a UM7204 PIN diode is used to monitor the intensity of each radiation pulse using the circuitry illustrated in Figure 2.1.

The PIN diode was calibrated using thermoluminescence dosimeters (TLDs) providing dose measurements with an accuracy of ±20%[5]. The characteristics of the TLD are described in Table 2.2, along with the PIN diode characteristics. The TLD is a calcium fluoride ribbon that is manganese doped (CaF_2:Mn). Four ribbons were placed in a TLD holder and wrapped in a 0.001-inch thick layer of aluminum foil.

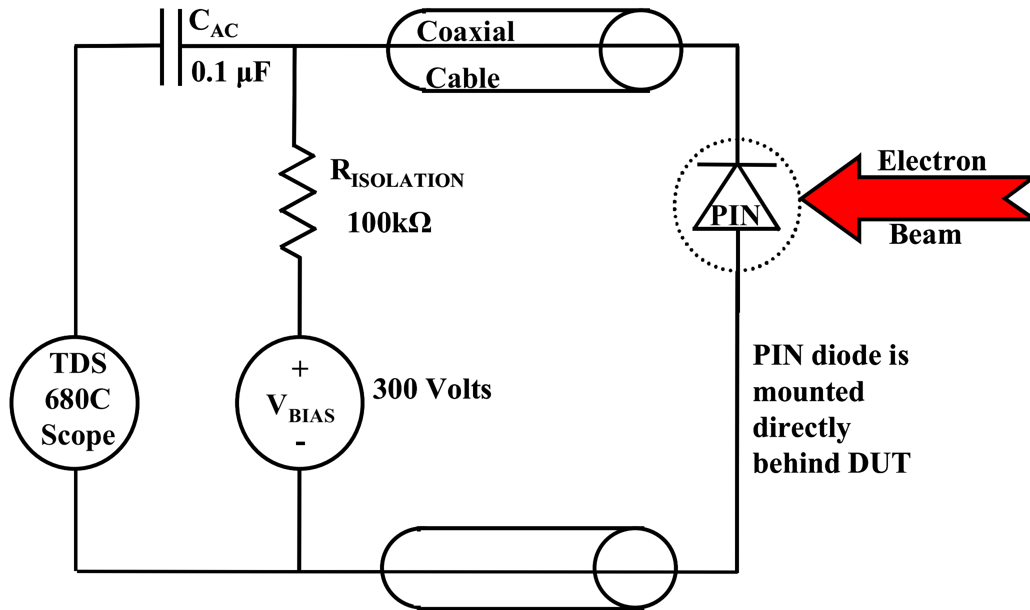

Figure 2.1. PIN diode circuit. A TLD is placed at the approximate Device Under Test (DUT) location to determine the dose of each pulse to calibrate the PIN diode.

Table 2.2
Dosimeter Description

Dosimeter	Type	Details
TLD	CaF_2: Mn doped chip	Chip Size: 1/8” x 1/8” x 1/32” (2 chips x 2 chips array)
PIN Diode	UM7204	V_R=400 Volts; Working bias of 300 Volts

The area of the PIN diode response is integrated at 10% of its peak power to obtain the dose response. The integrated area is then used in Equation 2.1 to obtain the variables, C_1 and C_2, by performing a least square fit to the measured dose. The average reading from the four TLD ribbons is then used to determine the dose from the radiation pulse, and in turn, used to calibrate the PIN diode.

$$\text{Dose}=(10)C_1(Area)C_2 \tag{2.1}$$

A positional table was used to position the PIN diode and the device under test (DUT) into the beam center. The intensity of the beam can then be altered by adjusting the table closer or farther from the beam exit port.

2.3 Test Fixture Description

The Schottky diodes were irradiated under various reverse biasing and beam intensities using the Naval Sea Systems Command (NAVSEA) Crane linear accelerator (linac) test facility. The test setup is shown in Figure 2.2. The data obtained are shown in section 2.4, with the photocurrent response under the various conditions of bias and beam intensity. After exposure, the devices were examined for signs of catastrophic failure.

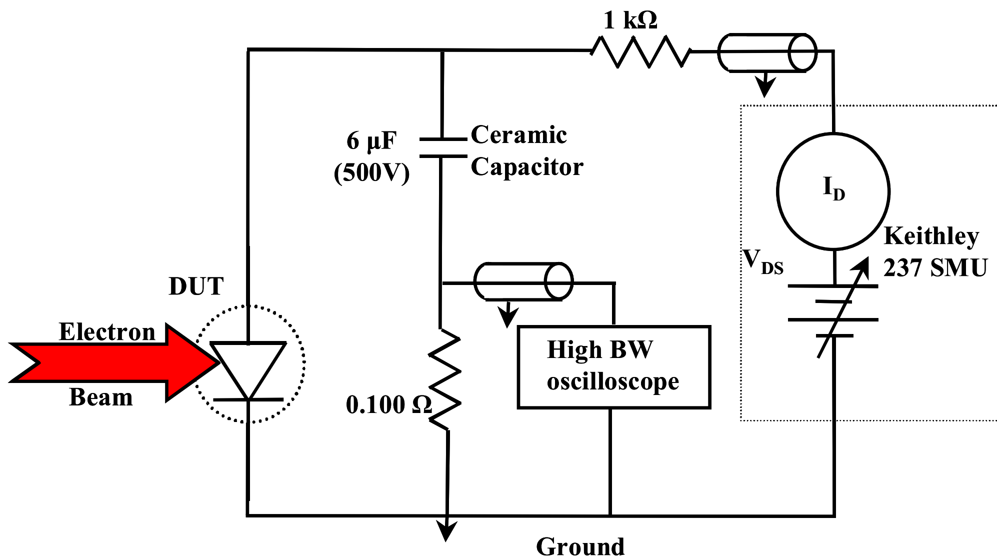

Figure 2.2. Test circuit used to measure photocurrent response.

The exposures were performed using a Faraday fixture with a beam Collimator (0.625 inch diameter hole) shielding the surrounding test circuit from the beam.

2.4 Test Procedure

The reverse bias was applied to the Schottky diodes during the test using a Keithley 237 Source-Measurement Unit, which allowed the leakage current to be measured during the pulse.

Test procedure was as follows: (1) place the Schottky diode onto test board; (2) verify functionality of device by monitoring reverse leakage current; (3) adjust the position of the table to set the correct dose rate; (4) apply a reverse bias while monitoring leakage current; (5) expose device to radiation pulse, at the same time recording photocurrent and PIN diode response; (6) test part for functionality; (7) repeat the test sequence with a different bias and/or beam intensity until the device fails catastrophically.

2.5 Experimental Results of 150-Volt Device

The photocurrent responses of the Schottky diodes, described in Table 2.1, were evaluated during exposure to 20-ns, 40 MeV electron pulses at various beam intensities ranging from 10^8 to $4x10^{11}$ rd(Si)/s as well as various reverse-bias levels (60V, 100V, 150V). The 150-Volt device has an epi-layer doping concentration and thickness of $8x10^{14}$ /cm^3 and 17.0 µm, respectively.

The photocurrent response of a single IR12CGQ150 diode when exposed to a 20-ns, $5x10^9$ rd(Si)/s electron pulse while reverse-biased at 100 V is shown in Figure 2.3. The device was still functional after exposure. The photocurrent response of the same device during exposure to a 20-ns, $1.31x10^{10}$ rd(Si)/s electron pulse while reverse biased at 100 V is shown in figure 2.4. From the photocurrent plot of Figure 2.4, it is evident that the device fails catastrophically, exhibiting a short circuit behavior after the pulse.

MIN
-4.22 A

MAX
10.98 A

PULSE PEAK
10.98 A

PULSE WDITH
[@ 3.38 A]
19.83 ns

DOSE RATE
5.06x10⁹ rd(Si)/s

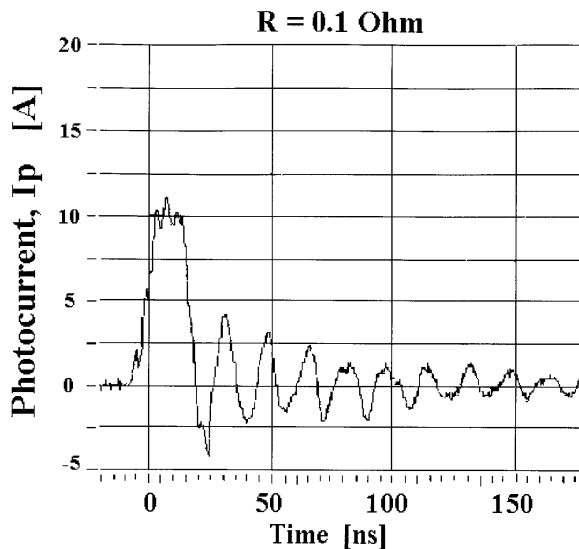

Figure 2.3 Photocurrent response, I_p, of an IR12CGQ150 when subjected to a 20-ns, $5x10^9$ rd(Si)/s electron pulse and reverse bias of 100 volts.

MIN
-0.384 A

MAX
27.11 A

PULSE PEAK
27.11 A

PULSE WIDTH
[@ 13.38 A]
26.4 ns

DOSE RATE
$1.31x10^{10}$ rd(Si)/s

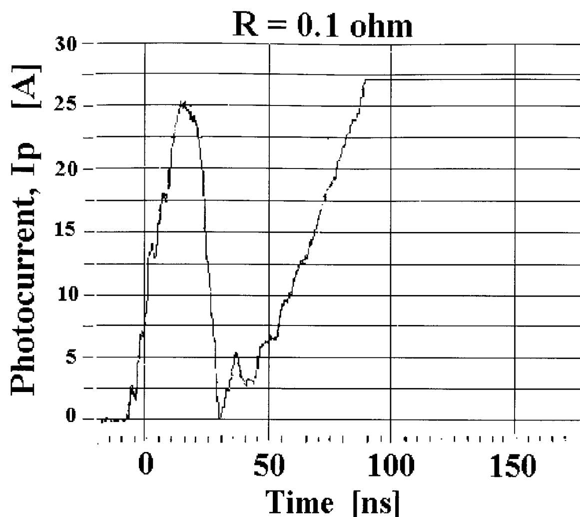

Figure 2.4 Photocurrent response, I_p, of an IR12CGQ150 when subjected to a 20-ns, $1.3x10^{10}$ rd(Si)/s electron pulse and reverse bias of 100 volts.

Figure 2.5 shows the peak photocurrent versus dose rate for various bias conditions (60V, 100V, 150V) from the IR12CGQ device. The plot shows the point at which the 150-volt device, burned out at the dose rate of $1.31x10^{10}$ rd(Si)/s. Figure 2.6 shows a die photograph with burnout sites. Note that the burnout sites are located at the guard ring.

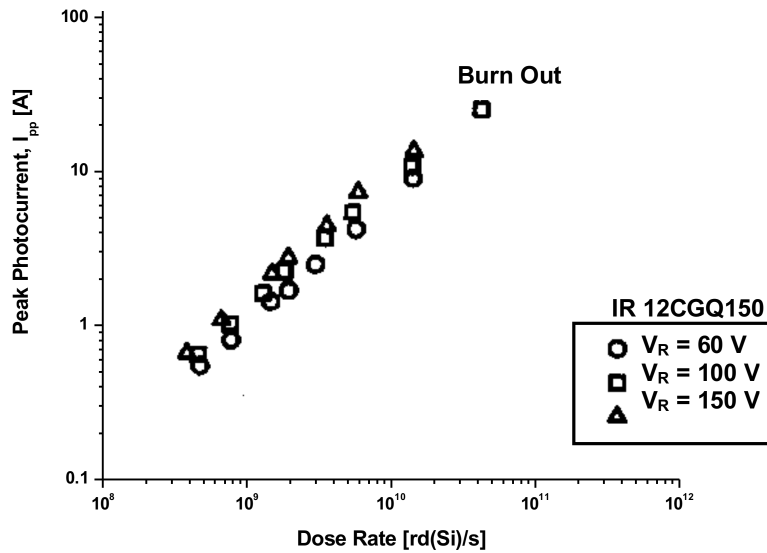

Figure 2.5. Peak current response, I_{pp}, measured from an IR12CGQ150 when reverse biased at 60, 100, and 150 Volts over a wide range of dose rates.

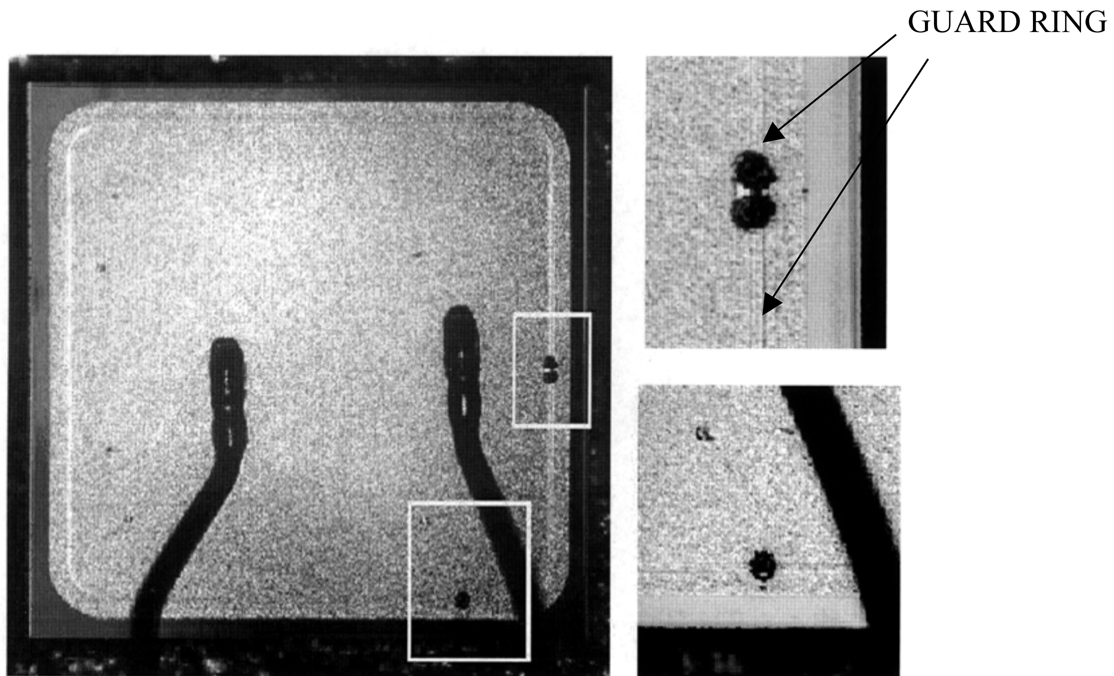

Figure 2.6 Die photograph and zoom showing failure at the guard ring as a result of electron pulse at guard ring.

2.6 Experimental Results of 45-Volt Device

The IR45CGQ045 is a 45-volt Schottky diode with a termination structure that is identical to the 150-volt device. The differences between these two devices lie in the doping concentration and thickness of the epi-layer. The epi-layer doping concentration and thickness are ~$6 \times 10^{15}/cm^3$ and 5.0 μm, respectively. The photocurrent response of this type of diode when exposed to a 20ns, 1.1×10^{10} rd(Si)/s electron pulse while reverse biased at 45 V is shown in Figure 2.7. None of the 45-V devices that were tested up to a maximum dose rate of 2×10^{11} rd(Si)/s while reverse biased at 45 V exhibited any signs of catastrophic failure.

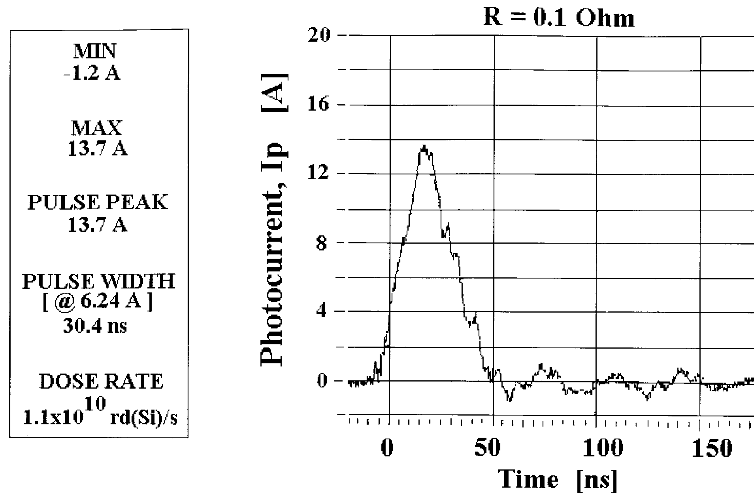

Figure 2.7 Photocurrent response, I_p, of an IR22CGQ045 when subjected to a 20-ns, 1.1×10^{10} rd(Si)/s electron pulse and reverse bias of 45 volts.

2.7 Experiment Supplement

Both new and failed devices were also examined using Scanning Capacitance Microscopy(SCM) and Scanning Electron Microscopy (SEM) at Dynamics Research Corporation. SEM cross-sections of failed devices reveals that they exhibited metal spiking at the guard ring portion of the device, shown in Figure 2.8.

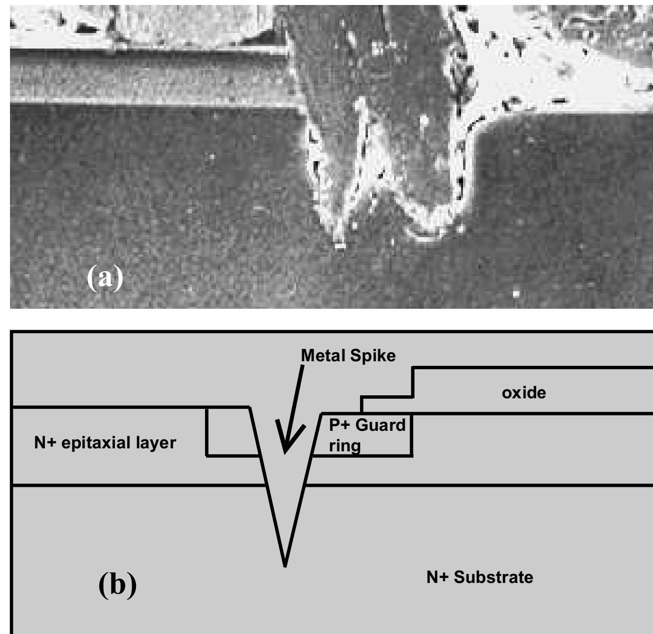

Figure 2.8(a) SEM Cross-sectional of contact aluminum spike through to the epi layer from a device that failed under test. **(b)** Diagram of relevant features of photograph

2.8 Conclusions from Experiment

Titus' conclusions are summarized as follows. It was demonstrated that Schottky diodes are susceptible to catastrophic failure when exposed to 20-ns, 40MeV electron pulses over a wide range of dose rates. The devices that failed exhibited a short circuit condition. The burnout was consistent with a localized breakdown inducing thermal runaway. Titus concluded that the photocurrent response is independent of die area, but is dependent on biasing and dose rate. Titus also concluded that the results showed that it is essential for system designers to evaluate the photocurrent response and burnout susceptibility prior to implementing Schottky diode systems where they may be subjected to a high dose-rate environment.

CHAPTER III

SIMULATION MODEL

3.1 Simulation Overview

Transient simulations were performed using a custom version of the SILVACO ATLAS PISCES-based device-simulation program that allows direct electron-hole-pair (EHP) generation throughout the device structure to simulate the effects of ionizing radiation[6]. The computing platform is a 128-processor Linux Beowulf-style cluster at Dynamics Research Corporation in San Diego, CA[7]. The 2-D structures for the devices were modeled using ATHENA, the SILVACO SUPREM4-based process simulator, with process recipes developed in collaboration with International Rectifier[6]. The structures are then revolved around a central axis, resulting in cylindrical volume solution structures. The simulations followed the experimental procedures by Titus, et al. as closely as possible[1].

3.2 Process Modeling

SILVACO's ATHENA process simulator tool was used to create the device structures for the simulations. The substrate and n-type epitaxial (Epi) starting material are defined with the resistivity calibrated to meet International Rectifier data sheets. Photolithography is modeled through the use of a masking step to form the diffused p-type guard ring. The SIMS-Verified Dual Pearson (SVDP) model is used to model ion implantation[8]. The annealing step of the guard ring implant is simulated to obtain an accurate doping profile. The Fermi diffusion model simulates the redistribution of dopants during thermal treatment as dependent on concentration gradients and internal electric fields[8]. The oxide is simply deposited; the growth is not modeled in this work. The Schottky barrier material is also defined, with the barrier height calibrated at a zero bias condition to meet the International Rectifier data sheet values. The aluminum contact and field plate over the oxide step is deposited and designated as the anode

electrode. The device structure obtained from ATHENA process models is then regridded using Devedit[8,9] to generate a better mesh for device-level simulations.

3.3 Device Modeling

3.3.1 Fundamental Semiconductor Equations

The device physics are modeled using numerical solutions to the set of fundamental partial-differential equations that link the electrostatic potential with the carrier densities. These equations have been derived from Maxwell's equations and consist of Poisson's equation, the continuity equation and the drift-diffusion transport equations. The spatial discretization of these equations is performed in order to apply them to the finite element grid that represents the simulation domain of the device. Poisson's equation relates the variations in electrostatic potential to the local charge densities:

$$div(\varepsilon \nabla \psi) = -\rho \tag{2.2}$$

where ψ is the electrostatic potential, ε is the local permitivity, and ρ is the local space charge density. The reference potential is defined by the intrinsic Fermi potential. The local space charge density is defined as the sum of the contributions from all mobile and fixed charges.

The electric field, $\vec{E}$, is obtained from the gradient of the potential:

$$\vec{E} = -\nabla \psi \tag{2.3}$$

The continuity equations describe the electron and hole densities as functions of the transport, generation, and recombination processes:

$$\frac{\partial n}{\partial t} = \frac{1}{q} div \overrightarrow{J_n} + G_n - R_n \tag{2.4}$$

$$\frac{\partial p}{\partial t} = \frac{1}{q} div \overrightarrow{J_p} + G_p - R_p \tag{2.5}$$

where n and p are the electron and hole concentration, $\overrightarrow{J_n}$ and $\overrightarrow{J_p}$ are the electron and hole current densities, G_n and G_p are the generation rates for electrons and holes, R_n and R_p are the total recombination rates for electrons and holes, and q is the magnitude of electron charge.

3.3.2 The Drift-Diffusion Transport Model

The drift-diffusion transport model is derived from the Boltzmann transport theory[13]. In this case the current densities are expressed in terms of the quasi-Fermi levels ϕ_n and ϕ_p and are modified to account for spatially varying lattice temperatures:

$$\overrightarrow{J_n} = -q\mu_n n\left(\nabla\phi_n + P_n\nabla T_L\right) \tag{2.6}$$

$$\overrightarrow{J_p} = -q\mu_p p\left(\nabla\phi_p + P_p\nabla T_L\right) \tag{2.7}$$

where μ_n and μ_p are the electron and hole mobility, and P_n and P_p are the absolute thermoelectric powers for the electrons and holes. P_n and P_p are modeled as follows:

$$P_n = \frac{k}{q}\left(\ln\frac{n}{N_c} - \frac{3}{2}\right) \tag{2.8}$$

$$P_p = \frac{k}{q}\left(\ln\frac{p}{N_v} - \frac{3}{2}\right) \tag{2.9}$$

The quasi-Fermi levels are linked to the potential, lattice temperature and the carrier concentrations through the following Boltzmann approximations:

$$n = n_i \exp\left[\frac{q(\psi - \phi_n)}{kT_L}\right] \tag{2.10}$$

$$p = n_i \exp\left[\frac{-q(\psi - \phi_p)}{kT_L}\right] \tag{2.11}$$

where n_i is the intrinsic concentration and T_L is the lattice temperature.
Effective electric fields are defined that allow the drift-diffusion equations to be written in the more conventional form:

$$\overrightarrow{E_n} = -\nabla(\psi + \frac{kT_L}{q}\ln n_i) \tag{2.12}$$

$$\overrightarrow{E_p} = -\nabla(\psi - \frac{kT_L}{q}\ln n_i) \tag{2.13}$$

3.3.3 Mobility Model

The carrier mobility is modeled with the Lombardi (CVT) mobility model[9]. In the CVT model, the temperature-dependent component, doping-dependent component and both the

transverse- and parallel-field dependent components of the mobility are combined using Mathiessen's rule:

$$\frac{1}{\mu_T} = \frac{1}{\mu_{AC}} + \frac{1}{\mu_{sr}} + \frac{1}{\mu_b} + \frac{1}{\mu_{\parallel}} \tag{2.14}$$

The first component, μ_{AC}, is the surface mobility component and is limited by scattering with acoustic phonons. The surface mobility component is dependent on the temperature and perpendicular electric field. The second component, μ_{sr}, is the surface roughness factor, and is dependent on the perpendicular electric field. The third component, μ_b, is the bulk mobility, and is limited by scattering with optical intervalley phonons. The bulk mobility is dependent on temperature. The last component, $\mu_{\parallel}$, is the parallel electric field mobility. The parallel electric field term accounts for carrier velocity saturation at high electric fields and is temperature dependent. This effect is necessarily accounted for by a reduction of the effective mobility since the magnitude of the drift velocity is the product of the mobility and the electric field component in the direction of the current flow. The parallel electric field model is based on the Caughey and Thomas expression and provides a smooth transition between low-field and high-field behavior[10].

The electron and hole saturation velocities, V_{nsat} and V_{psat} respectively, are calculated from the following temperature dependent model[3]:

$$V_{nsat} = V_{psat} = \frac{2.4 \times 10^7}{1 + 0.8 \exp\left(\frac{T_L}{600}\right)} \tag{2.15}$$

3.3.4 Carrier Generation-Recombination Models

In a homogeneously doped semiconductor with equilibrium concentrations of electrons, n_0, and holes, p_0, a steady state balance exists as:

$$n_0 \cdot p_0 = n_i^2 \tag{2.16}$$

If a semiconductor is excited by an external stimulus, the balance between generation and recombination is disturbed. Carrier generation-recombination is the process that attempts to return the semiconductor to an equilibrium condition. If an excess of carriers is generated then

recombination processes will dominate. If carriers are removed, then generation processes will dominate.

A modified Shockley-Read-Hall (SRH) recombination model is implemented that adds carrier concentration and temperature dependence into the SRH lifetime model[11,12]. The SRH recombination model accounts for the two-part process of phonon transitions that occur in the presence of traps within the band gap of the semiconductor. The SRH recombination is model follows:

$$R_{SRH} = \frac{pn - n_i^2}{\tau_{p0}\left[n + n_i \exp\left(\frac{E_{TRAP}}{kT_L}\right)\right] + \tau_{n0}\left[p + n_i \exp\left(\frac{-E_{TRAP}}{kT_L}\right)\right]} \qquad (2.17)$$

where E_{TRAP} is the difference between the trap energy level and the intrinsic Fermi level, T_L is the lattice temperature in Kelvin, and τ_{n0} and τ_{p0} are the electron and hole lifetimes. Rather than constant electron and hole lifetimes, as is conventionally the case in SRH models, the carrier lifetimes are made concentration and temperature dependent in this study through the implementation of Klaassen's lifetime model:

$$\frac{1}{\tau_{n0}} = \left(\frac{1}{K_{TN}} + \frac{1}{K_{CN}} \times N\right)\left(\frac{300}{T_L}\right)^{K_{GN}} \qquad (2.18)$$

$$\frac{1}{\tau_{p0}} = \left(\frac{1}{K_{TP}} + \frac{1}{K_{CP}} \times N\right)\left(\frac{300}{T_L}\right)^{K_{GP}} \qquad (2.19)$$

where N is the total local impurity concentration. The values used for the parameters K_{TN}, K_{CN}, K_{GN}, K_{TP}, K_{CP}, and K_{GP} are given in Table 3.1[6].

Table 3.1

Parameter Values for Equations 3.17 and 3.18

Parameter	**Value**	**Units**
K_{TN}	$2.5x10^{-3}$	s
K_{TP}	$2.5x10^{-3}$	s
K_{CN}	$3.0\ x10^{-13}$	cm^3/s
K_{CP}	$11.76\ x10^{-13}$	cm^3/s
K_{GN}	1.77	
K_{GP}	0.57	

3.3.4 Auger Recombination Model

Auger recombination becomes important in highly doped materials. Because of the high concentrations of excess carriers in a highly doped region, the probability of direct recombination is high. The Auger recombination model involves three carriers, as two carriers recombine and the third carries away the momentum and energy released by the recombination event[13]. Auger recombination is modeled using the expression:

$$R_{Auger} = AUGN\left(pn^2 - nn_i^2\right) + AUGP\left(np^2 - pn_i^2\right) \qquad (2.20)$$

where the model parameters AUGN and AUGP are defined in table 3.2[6].

Table 3.2

Parameter Values for Equation 3.19

Parameter	**Value**	**Units**
AUGN	8.3e-32	cm^6/s
AUGP	1.8e-31	cm^6/s

3.3.5 Impact Ionization Models

In a reverse-biased space-charge region, the free carriers are accelerated by the electric field. If a free carrier gains sufficient energy from the field before a collision with an atom, it

can break the bond between the atomic core and a bound electron. Thus, three carriers, the initial electron and the hole and electron created by the collision are free to leave the collision location. The carrier must gain adequate ionization energy, E_i, before the collision. This impact ionization process can be described by the following equation:

$$G = \alpha_n J_n + \alpha_p J_p \quad (2.21)$$

where G is the total generation rate of electron-hole pairs (ehps), $J_{n,p}$ are the current densities for electrons and holes and $\alpha_{n,p}$ are the ionization coefficients. The ionization coefficients follow the Selberherr model for the number of electron-hole pairs generated by a carrier per unit distance[14]:

$$\alpha_n = AN \exp\left[-\left(\frac{BN}{E}\right)\right] \quad (2.22)$$

$$\alpha_p = AP \exp\left[-\left(\frac{BP}{E}\right)\right] \quad (2.23)$$

where the coefficients AN, AP, BN, BP, β_n, and β_p, are functions of the lattice temperature. The temperature dependence of these coefficients is defined by the following equations:

$$AN = AN_{1,2}\left(1 + A.NT\left[\left(\frac{T_L}{300}\right) - 1\right]\right) \quad (2.24)$$

$$AP = AP_{1,2}\left(1 + A.PT\left[\left(\frac{T_L}{300}\right) - 1\right]\right) \quad (2.25)$$

$$BN = BN_{1,2}\left(1 + B.NT\left[\left(\frac{T_L}{300}\right) - 1\right]\right) \quad (2.26)$$

$$BP = BP_{1,2}\left(1 + A.PT\left[\left(\frac{T_L}{300}\right) - 1\right]\right) \quad (2.27)$$

The values for the parameters associated with the equations above are shown in Table 3.3[6].

Table 3.3

Parameters Values for Equations 3.23-3.26

Parameter	Value
A.NT	0.588
B.NT	0.248
A.PT	0.588
B.PT	0.248

3.3.6 Transient Modeling of Heat Generation and Conduction

The high current densities that result from the electron beam pulse cause local heating in the diode. The self-heating mechanisms are a factor in the failure of the device. Therefore, a physically rigorous thermodynamic model of the heat generation and conduction is necessarily implemented. The simulator uses Wachutka's model, consistent with the physical models considered in the isothermal drift-diffusion approximation[15]. The classical drift-diffusion approximations are extended to include a heat conduction equation involving heat sources and sinks. This heat conduction equation includes Joule and Thompson heating, and reflects the energy exchanged through radiative and nonradiative recombination and optical generation. The lattice heat flow equation has been added to the dynamic continuity equations for electron and hole flow:

$$c \cdot \left(\frac{\partial T}{\partial t} \right) = div\left(\kappa \vec{\nabla} T_L \right) + H \qquad (2.28)$$

where c is the heat capacitance per unit volume, κ is the thermal conductivity, and ***H*** is the heat generation rate.

Three heating and sinking sources are necessarily modeled: H_J, referred to as Joule heating, the Peltier and Thompson heating effects, H_{PT}, and the generation and recombination heating and cooling, H_{GR}[15]. These three components are summed to form the transient heat generation rate, *H*, as substituted in equation 3.27 above:

$$H = H_J + H_{PT} + H_{GR} \qquad (2.29)$$

The electron and hole Joule heat component was introduced by Gaur and Navon and models the heat generation resulting from the high electric current densities present after the ionizing pulse[16]:

$$H_J = \left[\frac{\left|\overrightarrow{J_n^2}\right|}{q\mu n} + \frac{\left|\overrightarrow{J_p^2}\right|}{q\mu p} \right] \tag{2.30}$$

The Peltier and Thompson effect models the heat exchange as particle currents traverse a temperature gradient in the material. The Peltier and Thompson heating component is given by:

$$H_{PT} = T_L\left(\overrightarrow{J_p}\nabla P_p\right) - T_L\left(\overrightarrow{J_n}\nabla P_n\right) \tag{2.31}$$

where P_n and P_p are given above in equations 3.7 and 3.8. The Peltier and Thompson term is determined by the magnitude of the gradients of the thermopowers. For this work, the heating component accounts for locally varying lattice temperature and strongly nonuniform doping concentrations; the transient recombination and regeneration heating and cooling component is modeled as[17,18]:

$$\begin{aligned} H_{RG} = q\left(R-G\right)&\left\{\left[T_L\left(\frac{\partial\phi_n}{\partial T}\right)_{n,p} - \phi_n\right] - \left[T_L\left(\frac{\partial\phi_p}{\partial T}\right)_{n,p} - \phi_p\right]\right\} \\ &- T_L\left[\left(\frac{\partial\phi_n}{\partial T}\right)_{n,p} + P_n\right]\nabla J_n - -T_L\left[\left(\frac{\partial\phi_p}{\partial T}\right)_{n,p} + P_p\right]\nabla J_p \end{aligned} \tag{2.32}$$

where P_p and P_n are given by equations 3.7 and 3.8, ∇J_n and ∇J_p are the gradients of the electron and hole currents and account for the time dependence.

3.3.7 Boundary Conditions

For a transient simulation, boundary conditions must be imposed at the boundary of the device structure and initial temperatures must be specified in order to obtain the temperature distribution in the solid. For this study, the initial temperature is defined at 300K. A Dirichlet (fixed temperature) thermal boundary condition is specified along the structure boundaries for the lattice heat flow equation[15]. The structure boundaries are at least two thermal penetration lengths away from the electrical heat source in agreement with the semi-infinite boundary criterion. The thermal penetration length, *L*, is found using equation 3.32

$$L = 2\sqrt{\alpha T} \tag{3.32}$$

where α is found using equation 3.33

$$\alpha = \frac{\kappa}{\rho c_p} \tag{3.33}$$

where ρ is the density and c_p is the specific heat for silicon. The thermal boundary conditions for the variable temperature are consistent with the isothermal models[13]. Along any boundary, the projection of the energy flux onto the unit normal vector N is a continuous function when passing across the surface. The boundary conditions for the carrier flow and the electric potential are extended to variable temperature by adding a temperature gradient dependence of the current,

$$\overrightarrow{J_{Tn}} = \mu_n \cdot n \cdot P_n \vec{\nabla} T \tag{3.34}$$

$$\overrightarrow{J_{Tp}} = \mu_p \cdot p \cdot P_p \vec{\nabla} T \tag{3.35}$$

into the drift diffusion equation, as shown in equations 3.7 and 3.8.

CHAPTER IV

RESULTS AND DISCUSSION

4.1 Results and Discussion Overview

Numerical simulation tools make it possible to model the physical mechanisms of a device during a pulse. The simulation results suggest that the diodes fail at the guard ring edge due to a depletion layer region collapse that effectively shorts the guard ring to the substrate. This low resistance path leads to high local current densities, resulting in thermal runaway. Simulation results also test techniques to improve the Schottky diode survivability.

4.2 Simulation Structure

During the initial simulation phase, the entire device was simulated, however it was evident that all of the pertinent physical activity during the pulse takes place at the guard ring area. Therefore, only the guard ring region was simulated, resulting in greater efficiency and accuracy, due to the fact that fewer mesh points are simulated in total, but more mesh points per area. The simulation structure is illustrated in Figure 4.1.

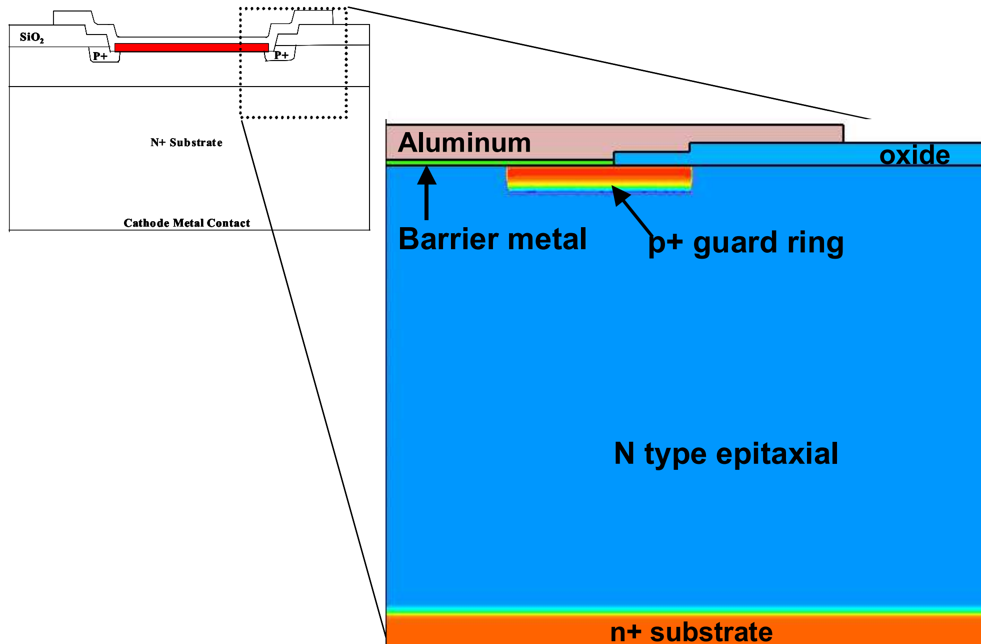

Figure 4.1 Simulation structure models the guard ring portion of the device.

4.3. Simulation Results

The device is exposed to an ionizing radiation pulse. The result of the pulse is uniform ionization of electron hole pairs in the potential gradient established by the biasing conditions. The pre-pulse potential gradients are shown in Figure 4.2. As the ehps are generated, the electrons flow toward the regions of higher potential, and the holes flow toward regions of lower potential. A cutline across the guard ring region, illustrated in Figure 4.2, shows the potential gradients that determine the local current flow and direction, shown in Figure 4.3. From Figure 4.3, it is evident that electrons generated in and underneath the guard ring will flow toward the outside edge of the device and down toward the cathode (direction shown by arrow in Figure 4.2).

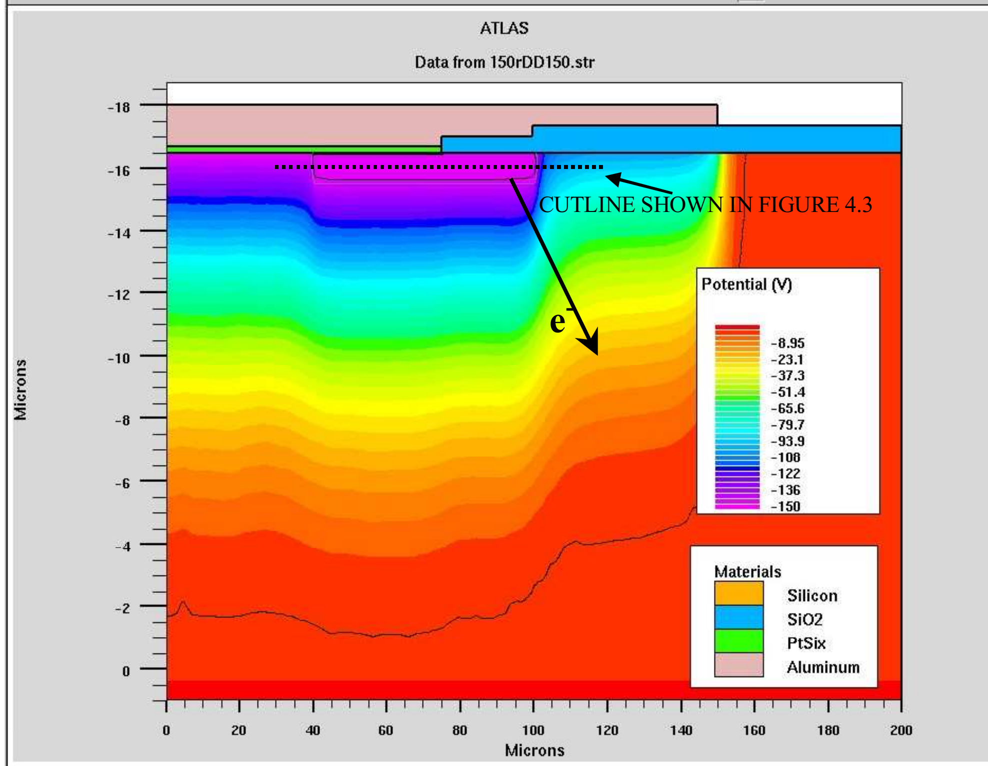

Figure 4.2 Pre-pulse Potential contours of Schottky diode biased at –150 Volts.

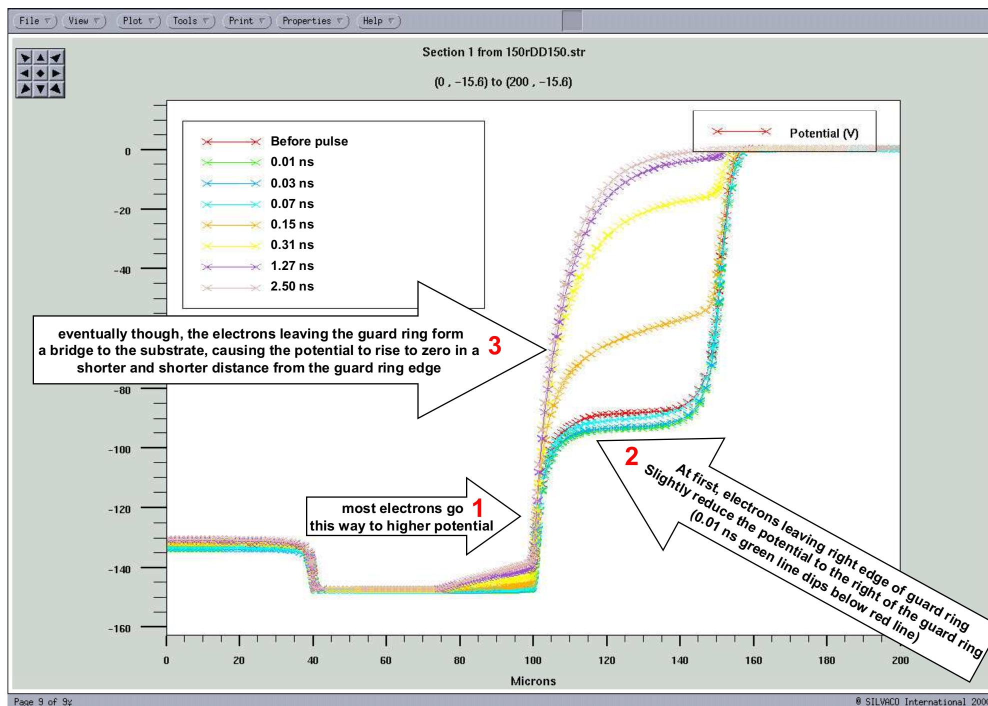

Figure 4.3 Cutline showing potential gradients across guard ring region.

At first, the electrons leaving the right edge of the guard ring and surrounding areas slightly reduce the potential to the right of the guard ring. Eventually, the electrons leaving the guard ring area form a 'bridge' of electrons to the n^+ substrate, causing the potential to rise to zero at shorter and shorter distances from the guard ring edge, as shown in Figure 4.3. The formation of this bridge is shown in the free electron density plot sequence of Figure 4.4. Figure 4.5 shows the simulated depletion region of the 150-volt device prior to the pulse and 0.03 nanoseconds into the pulse, zoomed to the guard ring region. The epi layer boundary is at location y=0. This higher potential gradient over a short distance equates to high local electric fields and current densities, forming a current filament. A rise in local temperature results from the high electric field and high local current densities at the outside edge of the guard ring as shown in Figure 4.6.

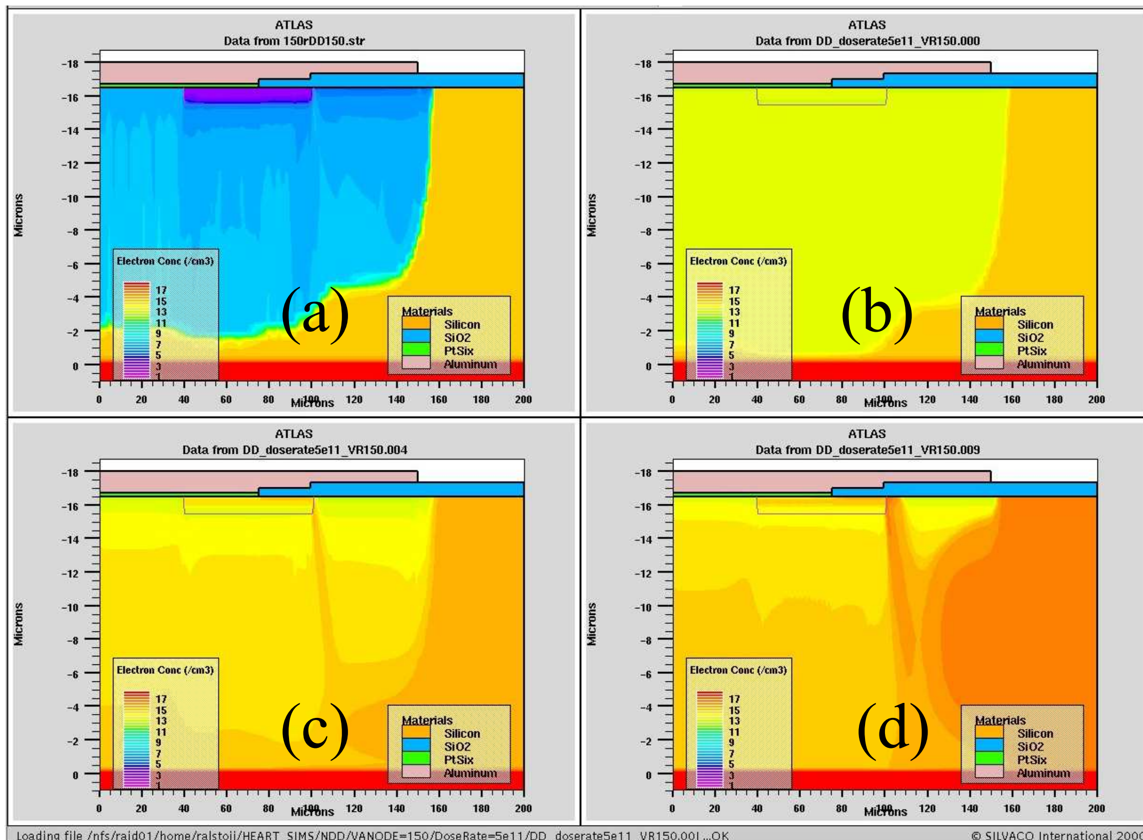

Figure 4.4 Time Sequence showing the formation of the electron bridge, effectively shorting the guard ring to the n^+ substrate (a) t=0, (b) t=0.01 ns, (c) t=0.31ns, (d) t=7.7ns.

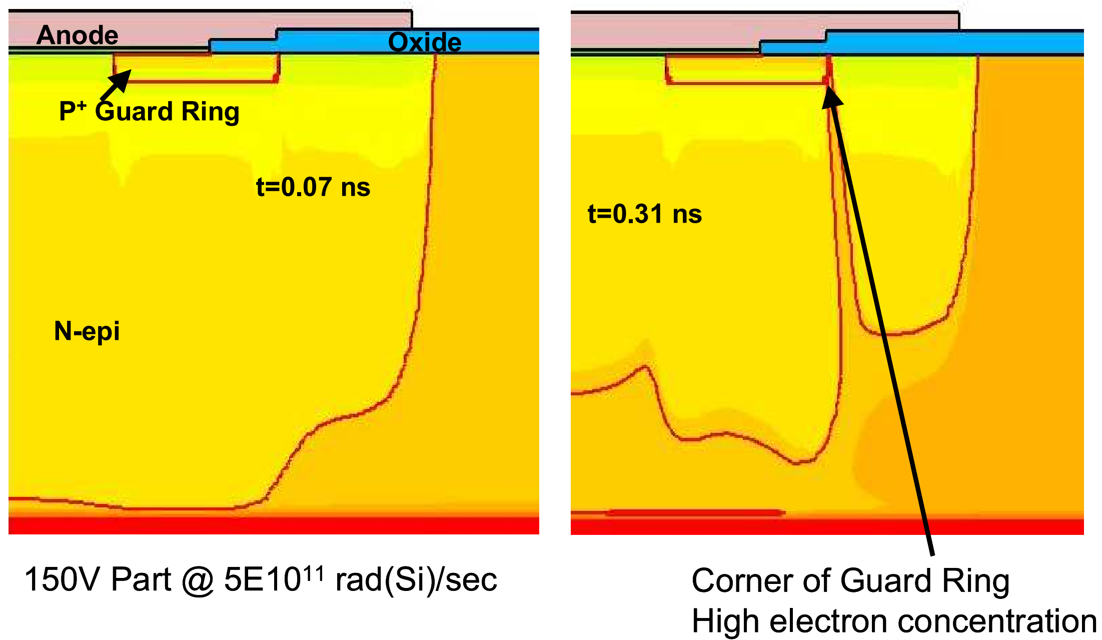

Figure 4.5 Depletion region (a) before and (b) 0.31 nanoseconds into the pulse

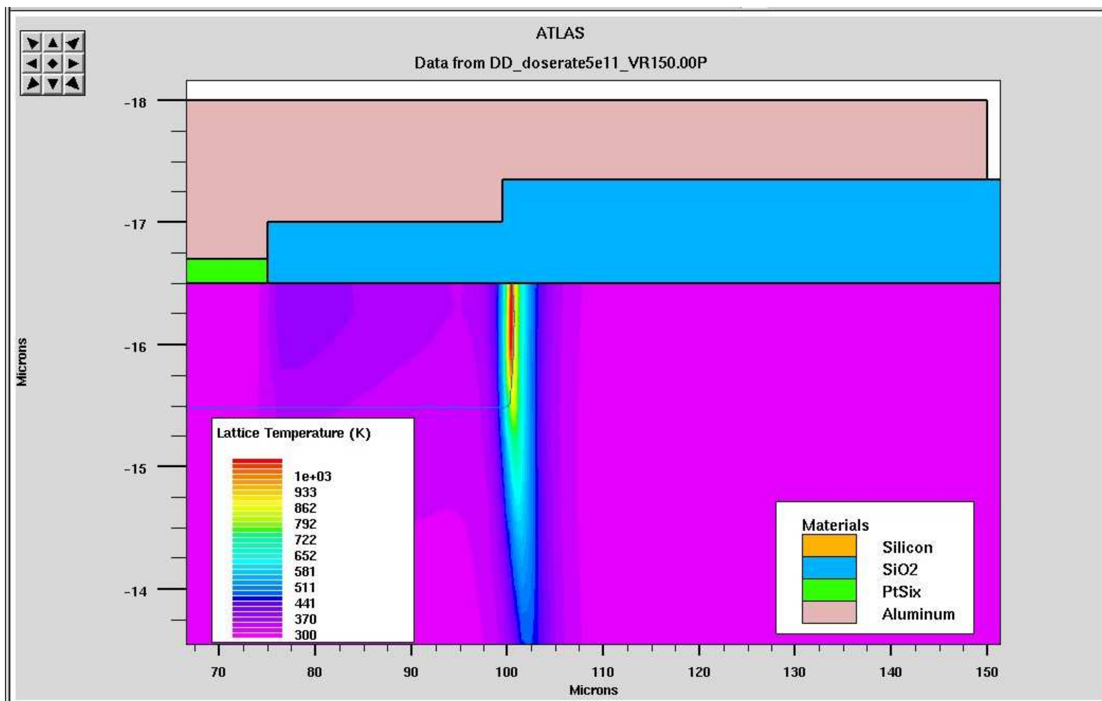

Figure 4.6 Local temperatures at t=17ns after pulse begins, zoomed to guard ring

4.4 Breakdown Discussion

Breakdown of the guard-ring p+n junction occurs by current localization due to the low resistance coefficient of silicon at the junction beyond a critical temperature, known as the intrinsic temperature, T_i[19-25]. At the temperature Ti, the thermally generated carrier concentration is equal to the dopant concentration on the n-type side of the p+n junction, n_d. Therefore, T_i can be calculated from the solution to the following equation[22]:

$$n_d = 1.69 \times 10^{19} \left(\frac{T_i}{300} \right)^{3/2} \exp\left(\frac{-E_G}{2kT_i} \right) \tag{4.1}$$

At temperatures below T_i, the carrier concentration is relatively insignificant, however, at temperatures above T_i, the carrier concentration rises exponentially with temperature. Thus, the consequence of localized heating in the current filament at the guard ring edge depends on whether or not the filament temperature exceeds T_i. At the intrinsic temperature, a "mesoplasma" is formed at the outside edge of the guard ring[26,27]. A factor of the mesoplasma is the thermal conductivity property of silicon, varying inversely with temperature. As a result, the temperature buildup during mesoplasma formation is assisted by the concurrent reduction in thermal conductivity of the silicon. This is a regenerative process since increased current flow is coupled with an increase in filament temperature[23]. In the case of the Schottky diode, the mesoplasma is responsible for a low resistance path for the generated ehps. The establishment of the mesoplasmas usually results in the failure of the device[28]. The overall process is field initiated and thermally terminated. It is important here to note the fact that the failed devices exhibited spiking of the metal at the guard ring region, shown in Figure 2.8. Thus, the critical temperature required to initialize the breakdown in the guard ring p+n junction region, T_i, can be used as the threshold figure of merit to determine whether the simulated devices survive or fail as a result of the electron pulse[25]. For the 150-Volt Schottky diode studied in this work, T_i is found using equation 4.1 to have a value of 585K. The intrinsic temperature versus doping level is plotted in Figure 4.7. The dopant concentration versus the intrinsic carrier concentration along a cutline through the p+n junction forming the guard ring is shown in Figure 4.8, showing the loss of the junction.

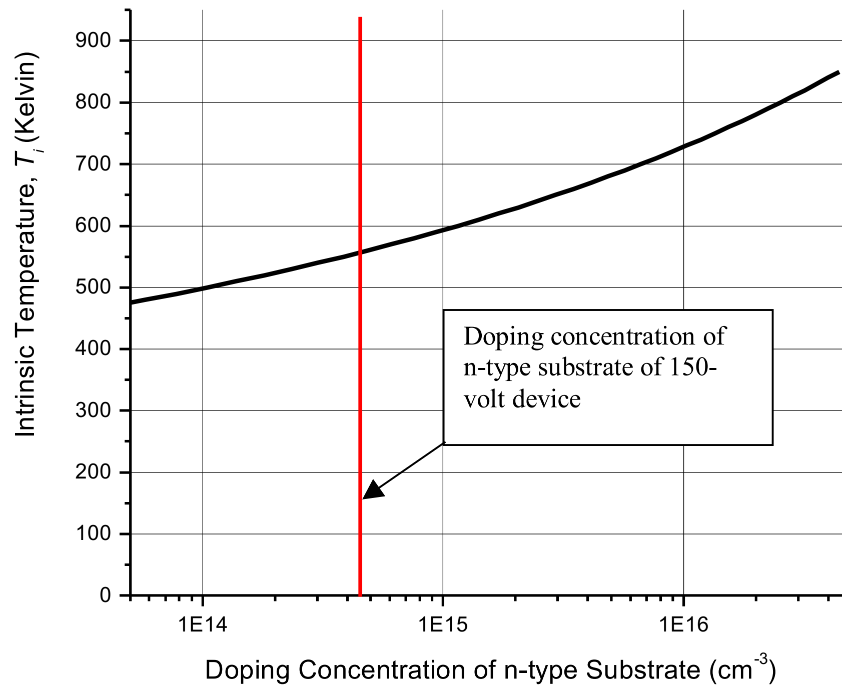

Figure 4.7 Intrinsic temperature, T_i, versus doping level of n-type substrate. Doping level of n-type substrate of 150-volt device shown by a red line.

When the local lattice temperature reaches the intrinsic temperature, T_i, the edge-termination-structure p+n junction breaks down, and consequently the entire device fails due to the parallel design of the Schottky portion and edge structure diodes, shown previously in Figure 1.4. The location of the simulated device breakdown is consistent with observed failure locations found in experimental analysis shown in Figure 2.6.

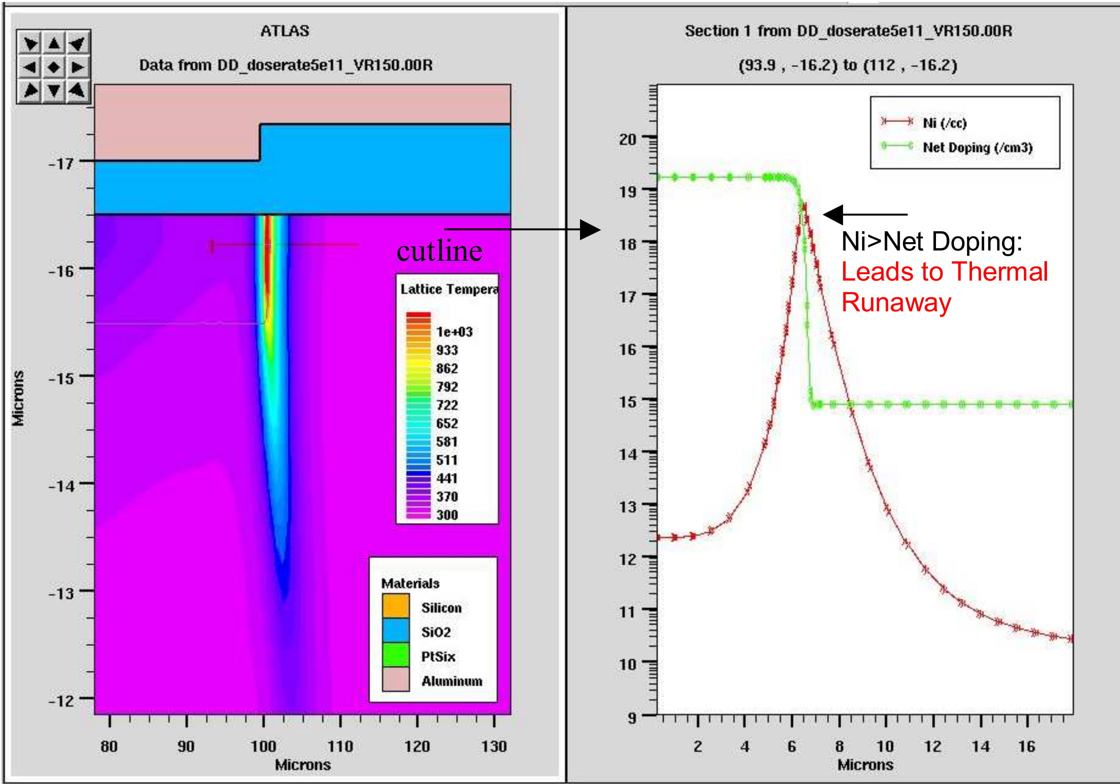

Figure 4.8 Cutline through p+n junction showing doping concentrations versus the thermally generated intrinsic carrier concentration, N_i. From this Figure it is evident that N_i is much greater than the n-type epi layer, and is responsible for junction breakdown.

A separate series of simulations solely modeling a simple p+n junction were performed to assure the validity of the breakdown criteria. The temperature breakdown validation simulation was performed on a 2.0x0.1x1.0 micron diode structure, biased at 1.0 V on the p-type anode, with the identical doping concentrations as the termination structure and epi layer ($8x10^{14}/cm^3$) concentrations in the Schottky diode, illustrated in Figure 4.9. The results of the junction break down are shown in Figure 4.9 by the increased current flow and are in good agreement with the calculated value of 585K without any calibration.

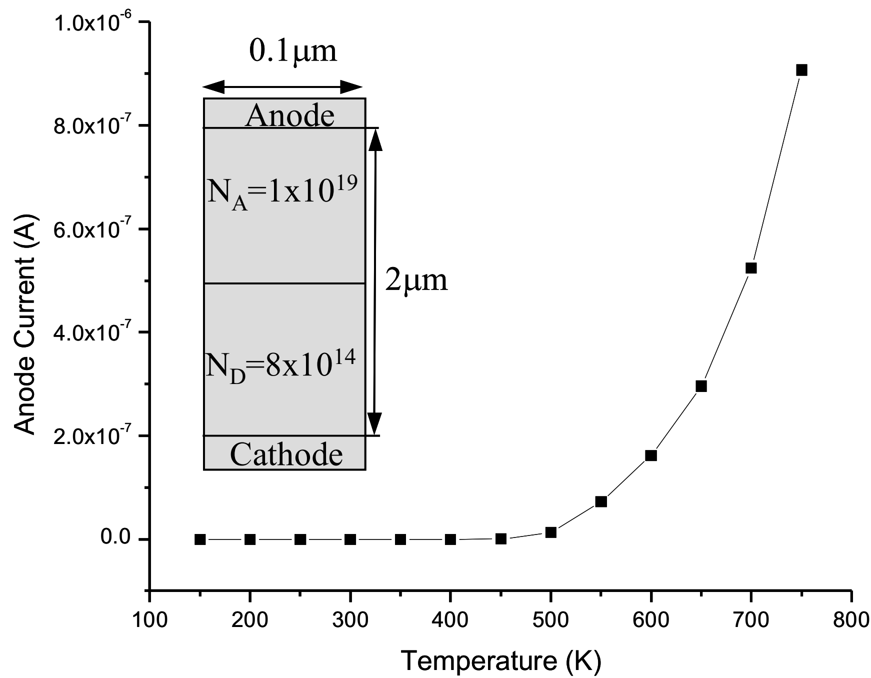

Figure 4.9 Illustration of p+n junction and a plot of its simulated current vs. temperature

4.4 Device Survivability Discussion

It was found that the lattice heating and subsequent breakdown are dependent on three conditions: the depletion region volume, the magnitude of the electric field across the guard ring, and the doping level of the epi layer. Firstly, the volume of the depletion region is governed by the size of the epi layer as well as the reverse biasing conditions across the diode. The depletion region is the collection volume supplying the breakdown current. The collection volume is directly proportional to the off-state bias as well as the thickness of the epi layer. Reducing the epi layer thickness would, however reduce the voltage handling capability of the diode (Equation 1.1). The second factor is the magnitude of the electric field (i.e., voltage drop) that is responsible for directing the current across the p+n junction that forms the guard ring. This electric field controls the energy levels of the charged carriers and governs the heat transfer to the lattice and subsequent lattice heating. Therefore, a reduction in the off-state bias may increase the part's survivability by reducing the magnitude of the localized electric field that occurs during the radiation pulse. The peak temperatures and photocurrent response versus time

during a $5x10^{11}$ rd(Si)/s pulse for the 150-volt device with an off-state bias of 75 and 150 volts are compared in Figure 4.10a and 4.10b.

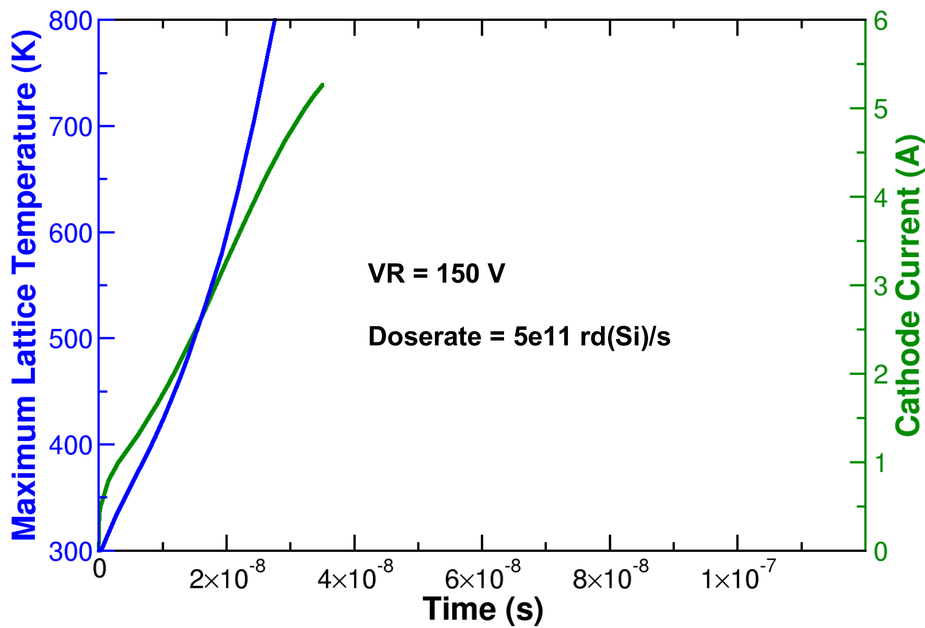

(a)

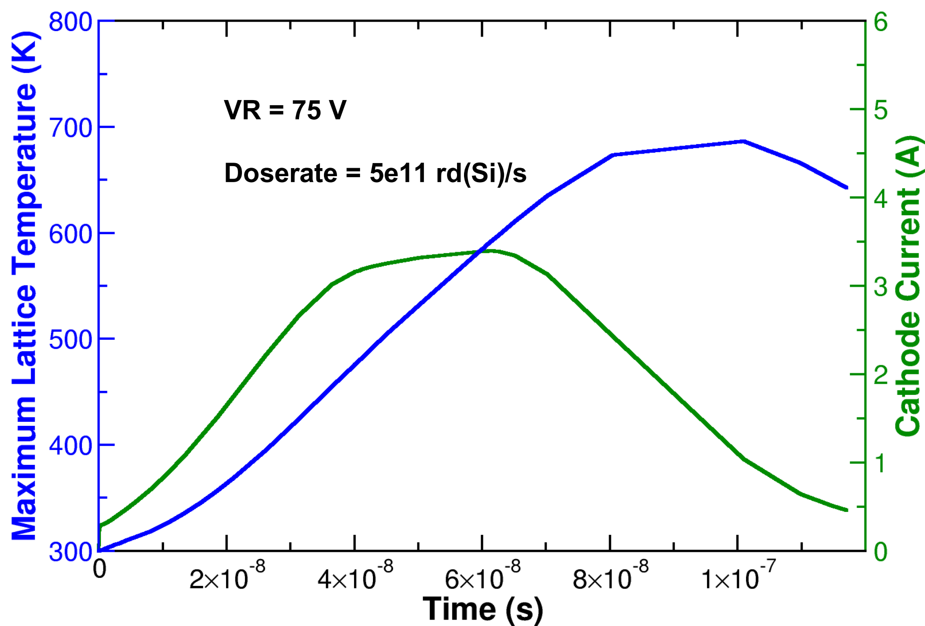

(b)

Figure 4.10 Current and peak temperatures versus time **(a)** for the 150-volt device reverse-biased at 150 Volts and **(b)** the 150-volt device reverse-biased at 75 Volts.

Lastly, the breakdown temperature is dependent on the doping of the lower-doped n-side of the p+n junction. If the doping on the n-side is increased, the breakdown temperature would also increase. The doping concentration of the 45-V device is $6x10^{15}$ /cm^3, resulting in the T_i for the 45-V device of 700K, 115˚ higher than that of the 150-volt device from Equation 4.1 and shown in Figure 4.11. This higher intrinsic temperature, combined with the lesser potential drop across the p+n guard ring termination structure, allows the 45-volt device to survive much higher dose rates. None of the simulated 45-volt devices met the temperature criteria that would result in a catastrophic failure.

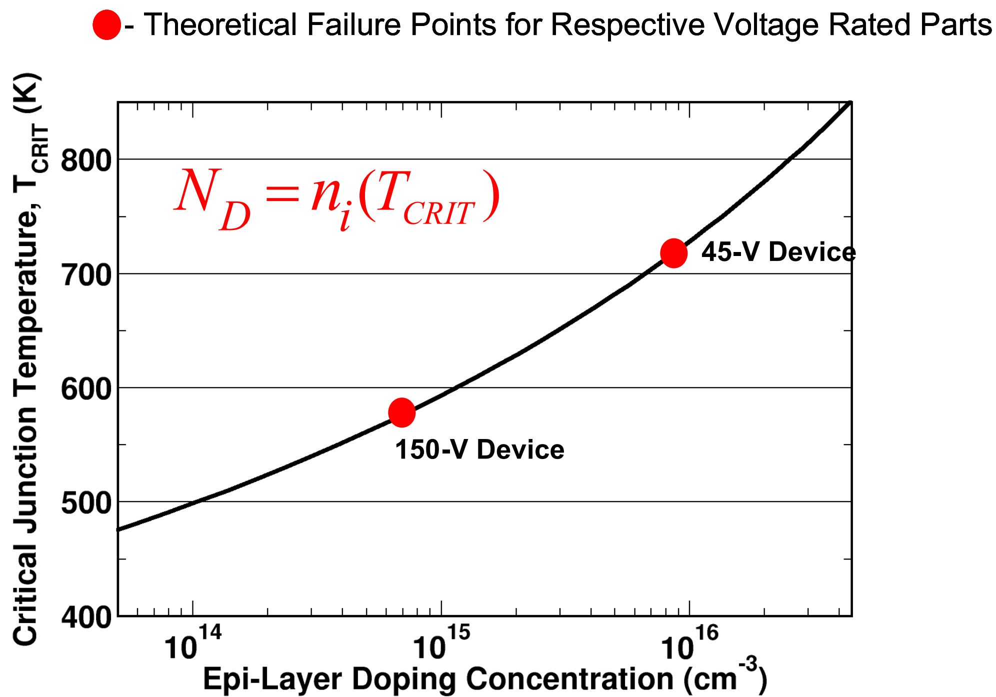

Figure 4.11 Current and peak temperatures versus time (a) for the 150-volt device reverse-biased at 150 Volts and (b) the 150-volt device reverse-biased at 75 Volts.

From these results it can be concluded that an increase in epi-layer doping concentration, in correlation with a reduction of the off-state bias increases the Schottky device survivability during ionizing radiation. The temperatures generated at the guard-ring pn junction during and shortly after a 20-ns, $5x10^{11}$ rd(Si)/s pulse are shown in Figure 4.13 for the 150-volt and 45-volt

rated devices. Lower peak junction temperatures are generated when the devices are pulsed at a lower off-state bias condition. Figure 4.13 also shows the junction temperatures during the pulse for the 45-volt and 150-volt rated devices biased at 1/2 of their respective rated voltage. Also the intrinsic temperatures for the two devices are compared in Figure 4.13.

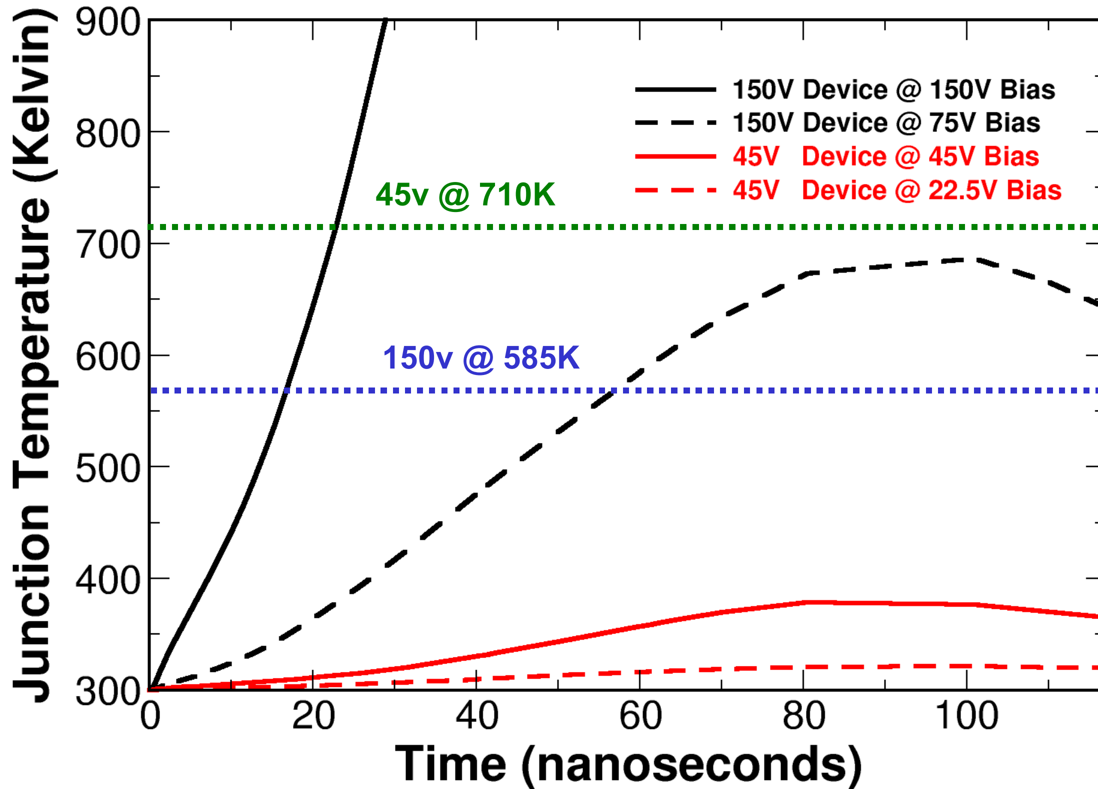

Figure 4.12 Plot of simulated temperatures generated at the guard-ring pn junction during and shortly after a 20-ns, $5x10^{11}$ rd(Si)/s pulse are shown for the 150-volt and 45-volt rated devices.

CHAPTER V

CONCLUSIONS

As discussed in Chapter II, Titus, et al. reported the failure of power Schottky diodes as a result of exposure to a 20-ns, 40-MeV electron pulse. Numerical models, as described in Chapter III, were used in this work to investigate the physical mechanisms responsible for the failure. The simulation results suggest that the diodes fail at the guard ring edge due to a depletion layer collapse, creating a low resistance path. This low resistance pathway leads to high local current densities resulting in elevated temperatures in the p+n junction that composes the guard ring.

A process for design-space exploration for power devices exposed to pulsed radiation is established. A critical temperature, T_i, can be used to determine device breakdown at the p+n junction that forms the guard ring. The temperature, T_i, is the temperature at which the thermally-generated carrier concentration rivals the doping concentration on the n-type side of the junction.

The lattice heating and subsequent breakdown is dependent on the magnitude of the voltage drop across the guard ring p+n junction. Therefore, a reduction in the off-state bias may increase the parts survivability by reducing the magnitude of the localized electric field that occurs during the radiation pulse. Also, the breakdown temperature, T_i, is dependent on the doping of the lower-doped n-side of the p+n junction. The existing 45-volt has a doping concentration of $6x10^{15}$ /cm^3, resulting in the T_i, for the 45-volt device, of 700K, 115° higher than that of the 150-volt device. This higher intrinsic temperature, combined with the fact that the magnitude of the electric field across the p+n guard ring termination structure is much lower and the smaller depletion volume, allows the 45-volt device to survive much higher dose rates. If the doping on the n-side is increased, the temperature at which breakdown occurs would also necessarily increase.

A device could be designed to withstand dose rate pulses on the order of $5x10^{11}$rd(Si)/s by manipulating the voltage drop across the guard ring as well as the thickness and doping concentration of the epi layer.

REFERENCES

[1] J. L. Titus, G. Bloomfield, J. E. Smith, S. Skinner, J. Ciezki, "Dose Rate Response of Reverse-Biased Power Schottky Diodes," To be published in Journal Radiation Effects, 2002.

[2] IEEE Transactions on Nuclear Science, IEEE Journal December issues; Papers from the Nuclear and Science Symposium (NSS)

[3] E.H. Rhoderick, Metal-Semiconductor Contacts, Clarendon, Oxford, 1978

[4] S.M. Sze, Physics of Semiconductor Devices, ISBN-0-472-05661-8, John Wiley and Sons, Inc., 1981.

[5] Intersil Corporation, Discrete Products Datasheet, http://www.intersil.com, June 1998

[6] ATLAS User's Manual, SILVACO International, February 2000.

[7] Chance Reschke, Thomas Sterlind, Daniel Ridge, Daniel Savarese, Donald Becker, and Phillip Merkey. A Design Network Topologies for the Beowulf Parallel Workstation. Proceedings Fifth IEEE International Syposium on High Performance Distributed Computing, 1996.

[8] ATHENA, User's Manual, Device Simulation Software, SILVACO International, 1998.

[9] Lombardi et al, "A Physically Based Model for Numerical Simulation of Non-Planar Devices", IEEE Trans. On CAD. Nov. 1988, p.1164

[10] D.M. Caughey and R.E. Thomas, "Carrier Mobilities in Silicon Emperically Related to Doping and Field", Proceedings of IEEE 55, pp. 2192-2193. 1967.

[11] D.B.M.. Klaasen, "A Unified Mobility Model for Device Simulation – I. Model Equations and Concentration Dependence", Sol. St. Elec., Vl 35, No. 2, pp.953-959, 1992

[12] D.B.M.. Klaasen, J.W. Slotbloom "A Inified Mobility Model for Device Simulation – II. Temperature Dependence of Carrier Mobility and Lifetime", Sol. St. Elec., Vl 35, No. 2, pp.961-9967, 1992

[13] S. Selberherr, Analysis and Simulation of Semiconductor Devices. Wien, Austria; Springer, 1984, Section 5.1

[14] A. G. Chynoweth, " Ionization Rates for Electron Holes in Silicon", Phys. Rev., 109, pp.1537-1540, 1958.

[15] G. K. Wachutka, "Rigorous Thermodynamic Treatment of Heat Generation and Conduction in Semiconductor Device Modeling", IEEE Trans. On Computer-Aided Design, Vol., 9, NO. 11, November 1990

[16] S.P. Guar and D.H. Navon, "Two-dimentional carrier flow in a transistor structure under nonisothermal conditions," IEEE Trans. Electron Devices, vol-ED-23, pp.50-57, 1976

[17] T.H. Geballe and G.W. Hull, "Seebeck effect in Silicon," J. Phys., vol. 98, pp. 940-947, 1955.

[18] M.E. Brinson and W. Dunstan, "Thermal conductivity and thermoelectric power of heavily doped n-type silicon," J. Phys., vol.C3 p.483-491, 1970.

[19] W. B. Smith, D.H. Pontius, and P.P. Budenstein, "Second Breakdown and damage in junction devices," IEEE Trans. Electron Devices, vol. ED-20, pp.731-744, 1973

[20] D.R. Alexander, "Electrical Overstress Failure Modeling for Bipolar Semiconductor Components," IEEE Trans. Comp. Hybrids Manuf. Technol., vol. CHMT-1, pp.345-353, 1978.

[21] F.J. Morin and J.P. Miata, "Electrical properties of Silicon containing arsenic and boron," Phys. Rev., 96, 28-35 (1954)

[22] S. K. Ghandhi, Semiconductor Power Devices. New York: Wiley, 1977.

[23] T Agatsuma, Turn Over Phenomena in n-v-n Si Devices and Second Breakdown in Transistors," IEEE Trans Electron Devices, ED-13, No. 11, pp. 748-753 (1966).

[24] T. Misawa, "Negative Resistance in p-n Junctions Under Avalanche Breakdown Conditions, Part I & II" IEEE Trans. Electron Devices, ED-13, No.1, pp. 1137-1151(1966)

[25] W.R. Runyan, "Silicon Semiconductor Technology," New York: McGraw-Hill, 1965.

[26] A.C. English "Physical Investigation of the Mesoplasma in Silicon," IEEE Trans. Electron Devices, ED-13, No 8/9, pp. 662-667 (1966)

[27] A.C. English, "Mesoplasmas and 'Second Breakdown' in Silicon Junctions," Solid State Electron., 6, pp. 511-521 (1963)

[28] I. Thompson and E.L.G. Wilkonson, "Destructive Breakdown in Large Area Phosporus Diffused high Voltage n+-p Junctions," Solid State Electron., 10, pp. 983-989 (1967).